CONDENSED MATTER PHYSICS

Discovery of a layered multiferroic compound $Cu_{1-x}Mn_{1+y}SiTe_3$ with strong magnetoelectric coupling

Chandan De[1,2]†‡, Yu Liu[1,2]†, Sai Venkata Gayathri Ayyagari[3]†, Boyang Zheng[1,2]†, Kyle P. Kelley[4], Sankalpa Hazra[3], Jingyang He[3], Sylwia Pawledzio[5], Subin Mali[2], Samaresh Guchaait[6], Suguru Yoshida[1,2], Yingdong Guan[2], Seng Huat Lee[1,2], Milos Sretenovic[7], Xianglin Ke[7], Le Wang[8], Mark H. Engelhard[9], Yingge Du[8], Weiwei Xie[10], Xiaoping Wang[5], Vincent H. Crespi[1,2], Nasim Alem[3], Venkatraman Gopalan[2,3]*, Qiang Zhang[5]*, Zhiqiang Mao[1,2,3]*

Multiferroic materials host both ferroelectricity and magnetism, offering potential for magnetic memory and spin transistor applications. Here, we report a multiferroic chalcogenide semiconductor $Cu_{1-x}Mn_{1+y}SiTe_3$ ($0.04 \leq x \leq 0.26$; $0.03 \leq y \leq 0.15$), which crystallizes in a polar monoclinic structure (*Pm* space group). It exhibits a canted antiferromagnetic state below 35 kelvin, with magnetic hysteresis and remanent magnetization under 15 kelvin. We demonstrate multiferroicity and strong magnetoelectric coupling through magnetodielectric and magneto-current measurements. At 10 kelvin, the magnetically induced electric polarization reaches ~0.8 microcoulombs per square centimeter, comparable to the highest value in oxide multiferroics. We also observe possible room-temperature ferroelectricity. Given that multiferroicity is very rare among transition metal chalcogenides, our finding sets up a unique materials platform for designing multiferroic chalcogenides.

INTRODUCTION

Ferroelectrics have a spontaneous polarization that can be reversed hysteretically by an external electric field. They play a pivotal role in a diverse range of technological applications, such as nonvolatile memory, photovoltaics, dielectrics, sensors, and actuators (*1–4*). Multiferroics are ferroelectric, or at least structurally polar, compounds that also have magnetic ordering, with potential applications in the electric field control of magnetization or vice versa (*5–7*). A large number of compounds, primarily from the pool of oxides, have been identified as multiferroics: $BiFeO_3$, $TbMnO_3$, $GaFeO_3$, $NiTeO_6$, $Fe_2Mo_3O_8$, $DyFeWO_6$, GaV_4S_8, and many others (*8–11*). Nevertheless, nanoscale device applications of multiferroics remain a challenge especially due to the disappearance of ferroelectric order in the two-dimensional (2D) limit (*12*, *13*). This challenge has been addressed recently through the discovery of 2D ferroelectrics in layered or van der Waals (vdW) materials such as T_d-WTe_2, 1T-$MoTe_2$, $(Mo/W)Se_2$, γ-InSe, (Ge/Sn)Te, $CuInP_2S_6$, and bilayer h-BN (*14–23*). These advances have inspired a search for new layered or vdW multiferroics among transition metal chalcogenides and halides (*24–27*).

A number of 2D or vdW magnetoelectric materials have been theoretically predicted, including $CuCrX_2$ (X = Se or S), MX_2 (M = Mn, Fe, and Ni; X = Cl, Br, and I) (*26*, *28–31*), bilayer VS_2 (*32*), VOI_2 (*33*), $(CrB_3)_2Li$ (*26*), and $Hf_2VC_2F_2$ (*25*, *32*, *34*). To date, however, only few layered materials, NiI_2, $CuCrP_2S_6$, and Te-doped WSe_2 (*35–37*) have been reported to be multiferroic. In NiI_2, a proper-screw helimagnetic ordering below 60 K breaks its inversion symmetry to a possible type II multiferroic state (*29*, *38*). $CuCrP_2S_6$, a magnetic derivative of $CuInP_2S_6$, is characterized by coexisting antiferroelectricity and antiferromagnetism, with spin-induced ferroelectricity below 30 K (*39*, *40*). Although a very recent study on this material shows evidence of switchable ferroelectricity at room temperature (*36*), its magnetic ground state at zero magnetic field has a fully compensated A-type antiferromagnetic (AFM) order and thus lacks a net magnetization (*35*). The absence of net magnetization in the multiferroic systems limits the magnetoelectric coupling, which is crucial for device applications. Despite the growing demand for 2D or layered multiferroic materials that exhibit both macroscopic polarization and net magnetization, there has been only a single report of such materials in layered chalcogenides, specifically Te-doped WSe_2 (*37*).

Here, we report the discovery of a layered, multiferroic chalcogenide semiconductor $Cu_{1-x}Mn_{1+y}SiTe_3$ ($0.04 \leq x \leq 0.26$; $0.03 \leq y \leq 0.15$) with a net magnetization, whose structural motif is distinct from those of MX_2 and $CuCrP_2S_6$. Single-crystal neutron diffraction refinements indicate a layered monoclinic polar structure with the space group of *Pm*; this noncentrosymmetry is then verified by optical second-harmonic generation (SHG). Piezoresponse force microscopy (PFM) reveals a clear hysteresis loop in the PFM amplitude and 180° phase switching at room temperature, suggesting that $Cu_{1-x}Mn_{1+y}SiTe_3$ is ferroelectric. This material displays a short-range AFM order below 60 K, which transitions into a long-range canted AFM order below 35 K (T_N). The canted magnetic moments produce a ferromagnetic (FM) component, leading to net magnetization and magnetic hysteresis below 15 K. Below T_N, we observe not only a large magnetodielectric effect but also a large magnetoelectric

[1]2D Crystal Consortium, Materials Research Institute, The Pennsylvania State University, University Park, PA 16802, USA. [2]Department of Physics, The Pennsylvania State University, University Park, PA 16802, USA. [3]Department of Materials Science and Engineering, The Pennsylvania State University, University Park, PA 16802, USA. [4]Center for Nanophase Materials Sciences, Oak Ridge National Laboratory, Oak Ridge, TN 37831, USA. [5]Neutron Scattering Division, Oak Ridge National Laboratory, Oak Ridge, TN 37831, USA. [6]Department of Physics and Astronomy, Howard University, Washington, DC 20059, USA. [7]Department of Physics & Astronomy, Michigan State University, East Lansing, MI 48824, USA. [8]Physical and Computational Sciences Directorate, Pacific Northwest National Laboratory, Richland, WA 99352, USA. [9]Environmental Molecular Sciences Laboratory, Pacific Northwest National Laboratory, Richland, WA 99352, USA. [10]Department of Chemistry, Michigan State University, East Lansing, MI 48824, USA.
*Corresponding author. Email: vxg8@psu.edu (V.G.); zhangq6@ornl.gov (Q.Z.); zim1@psu.edu (Z.M.)
†These authors contributed equally to this work.
‡Present address: Quantum Materials Science Unit, Okinawa Institute of Science and Technology, Okinawa 904-0495, Japan.

coupling, as manifested in a large magnetically induced electric polarization: $\Delta P \simeq 0.8\ \mu C/cm^2$ at 10 K and 9 T, comparable to the highest value reported for oxide multiferroics. These functional properties suggest that $Cu_{1-x}Mn_{1+y}SiTe_3$ is a layered multiferroic with electric polarization coupled to net magnetization. Our findings establish a unique platform for the study of multiferroics and provide clues for designing and synthesizing layered multiferroic chalcogenides needed for next-generation electronics and spintronics.

RESULTS

Crystal structure of $Cu_{1-x}Mn_{1+y}SiTe_3$

Single crystals of $Cu_{1-x}Mn_{1+y}SiTe_3$ were grown using the melt-growth method and the Te-flux method (see Materials and Methods). An optical image of a representative crystal is shown in the inset in Fig. 1B. The crystal composition varies depending on both the nominal composition of the source material and the specific growth conditions. Crystals exhibiting multiferroic properties were produced using the nominal composition of $CuMnSiTe_3$, which show slight variations in actual composition, expressed as $Cu_{1-x}Mn_{1+y}SiTe_3$, with $0.04 \le x < 0.26$ and $0.03 \le y \le 0.15$, and an average composition of $Cu_{0.82}Mn_{1.08}SiTe_{2.99}$ (see note S1 and table S1). These samples are characterized by Cu deficiency and Mn enrichment (denoted as Type A hereafter). The composition of this system can be further tuned by adjusting the nominal composition. Crystals with a Cu/Mn ratio close to 1 (Type B) or with a higher Cu content (Type C) can also be synthesized (see Materials and Methods, note S1, fig. S1, and table S1). However, this paper focuses exclusively on the Cu-deficient Type A samples as only this type exhibits multiferroic properties (see note S5 and fig. S10).

Room-temperature single-crystal x-ray (see note S3 and fig. S6) and neutron diffraction measurements on a Type A sample (S#1), when refined to a single-domain crystal structure, yields a monoclinic structure with a noncentrosymmetric space group *Pm* (no. 6), as depicted in Fig. 1A. The refined composition was $Cu_{0.844}Mn_{1.156}SiTe_3$, consistent with the average composition $Cu_{0.78}Mn_{1.10}SiTe_{3.02}$ measured using energy-dispersive x-ray spectroscopy (EDXS).

Broadly speaking, the structure of $Cu_{1-x}Mn_{1+y}SiTe_3$ comprises a series of close-packed Te layers that alternate with cation layers containing Si_2 dimers, Mn ions, and Cu ions along the *c* axis (Fig. 1A). Mn coordination to Te is octahedral, whereas Cu coordination to Te is tetrahedral; both coordination geometries have substantial distortion. The Si_2 dimers form ethane-like Si_2Te_6 units with Te neighbors. Streaks in the neutron and electron diffraction data (figs. S4 and S6) suggest the presence of stacking faults along the layering direction; careful scanning transmission electron microscopy (STEM) observation (Fig. 2C and fig. S3) suggests that these faults correspond to differences in the relative stacking order of the Te layers (see figs. S2 and S5, and note S2). Both x-ray and neutron diffraction data also suggest an occupancy of Mn on the Cu1 (2c: 0.10202, 0.33046, and 0.09915) and Cu2 (2c: 0.8749, 0.83109, and 0.90844) Wyckoff positions. Because of the significant difference in neutron scattering lengths between Mn (−3.73 fm) and Cu (7.72 fm), we can extract inequivalent site occupancy at the Cu1 and Cu2 sites to be ~21.7 and 9.7%, respectively (see note S3 and fig. S7). The refined atomic positions, lattice constants, site occupancy, and atomic displacement parameters at 300 K are summarized in table S2.

A lack of centrosymmetry in $Cu_{1-x}Mn_{1+y}SiTe_3$ was verified by the observation of optical SHG (see Fig. 2A for the measurement configuration). Figure 2B shows the SHG polar plot measured on a Type A sample (S#2), which can be fitted well with the point group *m* (corresponding to the space group *Pm*) assuming a multidomain model (see note S4). The second harmonic field amplitude responses of each domain variant considered are scaled with an area fraction and are coherently added to generate the net SHG intensity. Atomic-resolution STEM reveals an interesting multidomain stacking structure. Figure 2C shows the annular dark-field STEM (ADF-STEM) image along the [010] zone axis. In the inset in Fig. 2C, we present a magnified view overlaid with the projected *Pm* structure, which shows consistency with the Te atomic columns of one constituent stacking domain. The projected distance between Si and Mn falls below 60 pm, near the resolution limit of the STEM, so we were unable to resolve the positions of Si using STEM from this direction.

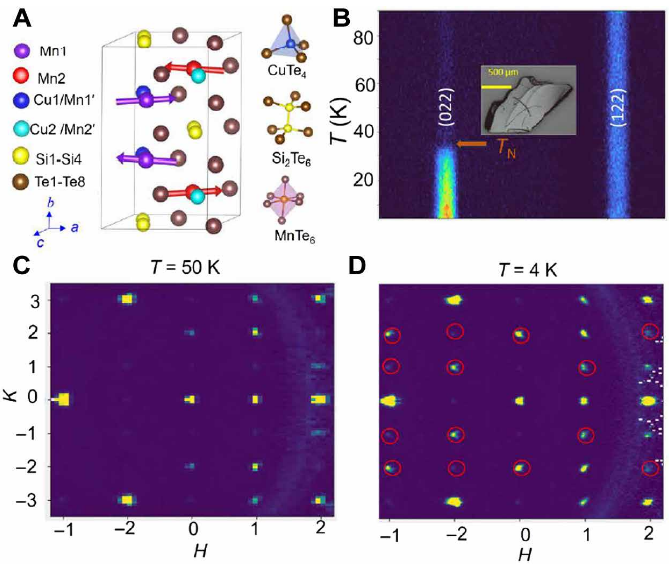

Fig. 1. Crystal and magnetic structure from single-crystal X-ray and neutron diffraction structure refinement for $Cu_{0.78}Mn_{1.10}SiTe_{3.02}$ (S#1). (**A**) Crystal and magnetic structure (left) and schematic of the chemical environment of Cu, Si, and Mn (right). (**B**) Temperature dependence of Bragg peaks (022) and (122). The single-crystal neutron diffraction patterns in the (HK4) plane collected at TOPAZ at (**C**) 50 K and (**D**) 4 K.

Electronic and magnetic properties of $Cu_{1-x}Mn_{1+y}SiTe_3$

Spectroscopic ellipsometry measurements (see fig. S8) indicate that the Cu-deficient $Cu_{1-x}Mn_{1+y}SiTe_3$ sample (S#2) is a semiconductor, with indirect and direct bandgaps of 1.26 and 2.50 eV, respectively. Its semiconducting nature is further supported by transport measurements, as discussed below. Using the *Pm* structure obtained from x-ray and neutron diffraction refinement and assuming no Mn occupation at Cu sites, we performed density functional theory (DFT) band structure calculations, revealing a semiconducting band structure with an indirect bandgap of 0.94 eV (see note S6 and fig. S11). The computational methods are detailed in the Materials and Methods section. Although DFT calculations typically underestimate bandgaps, the semiconducting nature is qualitatively correct. When considering partial Mn substitution at Cu sites, the electronic band structure continues to display semiconducting characteristics (see note S6), consistent with experimental observations.

Because the *Pm* structure allows for both the in-plane and out-of-plane components of electric polarization, which likely leads to ferroelectricity, we performed PFM studies on the Cu-deficient $Cu_{1-x}Mn_{1+y}SiTe_3$ sample (S#2) to examine its electric polarization switching. Figure 3A gives the surface topography of a piece of crystal (~50 μm in thickness) cleaved from the sample S#2 measured in PFM, showing a very low surface roughness, <200 pm. Figure 3 (B and C) shows the bias voltage–dependent amplitude and phase of the PFM response measured at room temperature, showing hysteresis in the voltage amplitude (Fig. 3B) and a corresponding 180° phase switch (Fig. 3C), suggesting room-temperature ferroelectricity. The coercive field of this sample is near the breakdown field, due to which a maximum achievable applied voltage was 4 V. This limitation of applied voltage prevents us from observing the amplitude saturation. Thus, for further confirmation of ferroelectric nature, we locally measure the hysteresis on crystals of different thickness. If the hysteresis behavior is

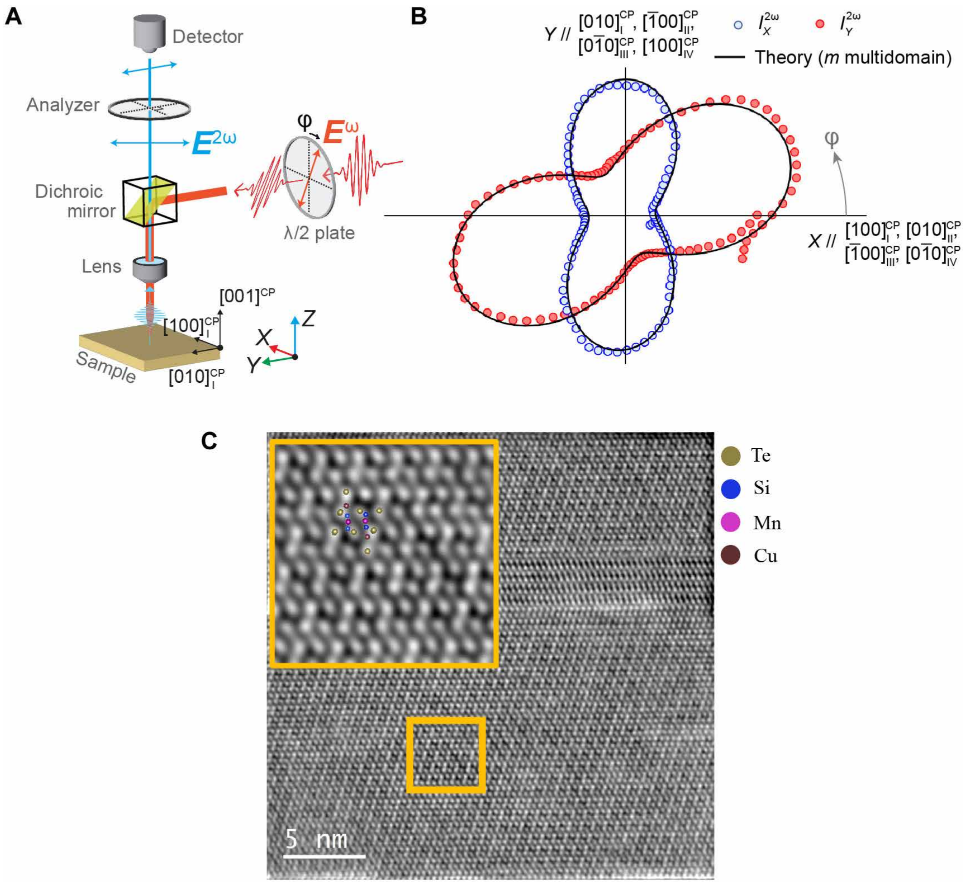

Fig. 2. SHG measurements for $Cu_{0.80}Mn_{1.03}SiTe_{2.92}$ (S#2) and STEM images for $Cu_{0.78}Mn_{1.10}SiTe_{3.02}$ (S#1). (**A**) SHG experimental setup showing the optical path of incident light (ω) and reflecting light from the crystal with 2ω frequency. The lab axes (*X*, *Y*, and *Z*), crystal physics (CP) axes of one of the four domains, and the relation between them are defined. (**B**) Polar plot for the intensity of *X*- and *Y*-polarized SHG light. The black continuous line shows the fitted pattern for point group *m*. (**C**) ADF-STEM image showing the Te atomic arrangement along the [010] zone axis. The inset shows the magnified view overlaid with the projected *Pm* structure. Additional information regarding the stacking faults is included in the note S2.

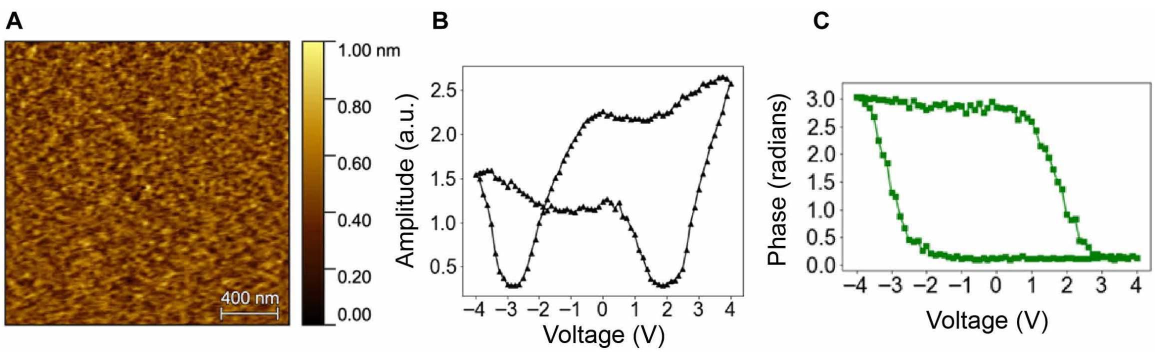

Fig. 3. PFM measurements on $Cu_{0.80}Mn_{1.03}SiTe_{2.92}$ (S#2). (**A**) Surface topography of the cleaved crystal measured using PFM. (**B**) PFM amplitude and (**C**) phase as a function of bias voltage measured at room temperature. a.u., arbitrary units.

truly an electrostatic effect, then we should observe marginal differences in the hysteresis loops when comparing thick versus thin crystals. However, we observe a large increase in the coercive field in a thick crystal (~0.5 mm in thickness, see fig. S12), suggesting that the measured effect is most likely a ferroelectric effect in nature for the sample (see note S7 for details).

We studied the magnetic behavior of $Cu_{1-x}Mn_{1+y}SiTe_3$ by magnetization, ac magnetic susceptibility, and specific heat measurements. Figure 4A presents the temperature dependencies of the magnetization measured under the zero-field cooling (ZFC) and field-cooling (FC) histories with a magnetic field of 0.1 T applied parallel and perpendicular to the *ab*-plane direction, respectively. The magnetization along the in-plane direction begins to increase rapidly below ~60 K, followed by a sharp transition at ~35 K. These magnetic transitions were also seen in the ac susceptibility measurements, as shown in Fig. 4B. Heat capacity measurements under zero field and a field of 1 T reveals a significant anomaly peak at 35 K, indicating that a long-range magnetic order emerges below ~35 K, whereas a short-range magnetic order develops between ~35 and ~60 K. The negative Curie-Weiss temperature extracted from the Curie-Weiss fit (see note S8 and fig. S13) suggests that the transition at ~35 K is of AFM characteristics. Neutron scattering measurements at low temperatures, combined with magnetization results, confirm that the system transitions to a canted AFM state below 35 K, as discussed below.

Furthermore, when the magnetic field is applied along the in-plane direction, the magnetization measured under the ZFC and FC histories was found to exhibit significant bifurcation below 15 K, which can be attributed to the FM component of the AFM state. The weak ferromagnetism below 15 K is further evidenced by the isothermal magnetization measurements presented in Fig. 4 (E to G), which reveal a noticeable magnetic hysteresis with a very small remanent magnetization [~0.06 bohr magnetons (μ_B)/formula unit (f.u.) at 2 K] at low temperatures for $H \parallel ab$ but not for $H \perp ab$ (Fig. 4E). Such an anisotropic magnetic hysteresis behavior can be well understood in terms of a canted AFM state. The slight canting of magnetic moments in the AFM state leads to a weak FM component, which accounts for the FM behavior below 15 K. The larger magnetization for $H \parallel ab$ compared to $H \perp ab$ (Fig. 4, F and G), as well as the magnetic hysteresis observed only for $H \parallel ab$ (Fig. 4E), indicates that the net magnetization of the canted AFM state is within the *ab* plane.

To find the magnetic structure below T_N (= 35 K), we performed single-crystal neutron diffraction measurements on a sample with the EDXS-measured average composition $Cu_{0.78}Mn_{1.10}SiTe_{3.02}$ (S#1) at 300, 50, 23, and 4 K. Figure 1 (C and D) compares the neutron diffraction patterns of the Bragg peaks in the (HK4) plane at 50 and 4 K. A few magnetic peaks were clearly observed at 4 K in this plane. Many other magnetic peaks in different planes were also observed. The temperature dependence of the representative magnetic peak (022), shown in Fig. 1B, indicates that the magnetic peak emerges below T_N, consistent with the magnetic transition probed by the magnetization, ac susceptibility, and heat capacity measurements presented above. No significant change in intensity or additional magnetic peaks were detected below 15 K where the FM behavior is observed, which, together with the heat capacity data (Fig. 4C), indicate that no additional magnetic transition occurs below 15 K. The presence of the FM behavior below 15 K can be attributed to the suppression of thermal fluctuation, which could lead to net magnetization of AFM domains.

There is no evidence for the ordered Mn1′ (or Mn2′) moments at the Cu1 (or Cu2) sites. The magnetic peaks are instrument-resolution

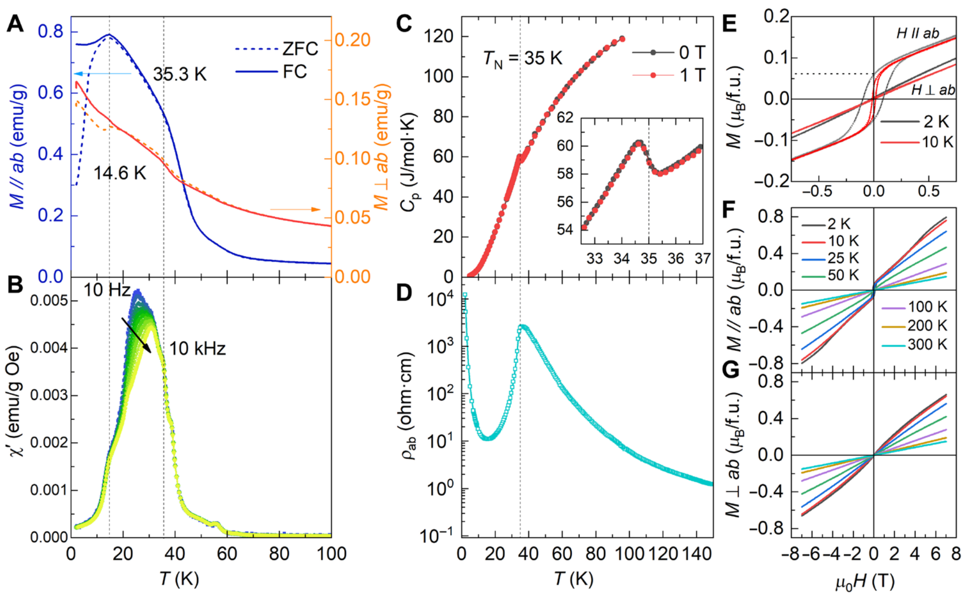

Fig. 4. Magnetization, ac magnetic susceptibility and resistivity measurements on $Cu_{0.80}Mn_{1.03}SiTe_{2.92}$ (S#2), and heat capacity measurement on $Cu_{0.79}Mn_{1.08}SiTe_{2.97}$ (S#3). (**A**) Temperature-dependent dc magnetizations (*M*) measured under both FC and ZFC histories with a magnetic field (0.1 T) parallel and perpendicular to the *ab* plane. emu, electromagnetic units. (**B**) Real part of ac magnetic susceptibility (χ') measured with a 0.1-T magnetic field perpendicular to the *ab* plane. (**C**) Temperature-dependent heat capacity measured under zero field and the field of 1 T. (**D**) Temperature-dependent in-plane resistivity. (**E**) Field sweeps of magnetization with the field parallel and perpendicular to the *ab* plane measured at 2 and 10 K. Field sweeps of magnetization with a magnetic field parallel (**F**) and perpendicular (**G**) to the *ab* plane at various temperatures.

limited, indicative of a long-range magnetic order below T_N. All the magnetic peaks can be indexed based on the high-temperature nuclear (chemical) unit cell with a magnetic propagation vector $\mathbf{k} = (0,0,0)$. The determined magnetic structure in $T < T_N$ is displayed in Fig. 1A. The Mn spins at both Mn1 and Mn2 sites are ferromagnetically aligned along the *a* and *c* axes but antiferromagnetically aligned along the *b* axis. Furthermore, the nearest-neighbor Mn1 and Mn2 spins are antiparallelly aligned. The magnetic space group is *Pm* (Belov-Neronova-Smirnova no. 6.18). The magnetic moment of Mn mainly points along the *a* axis, with the ordered moment of 2.66(18) μ_B at 4 K and 2.29(6) μ_B at 23 K, respectively. This refined colinear AFM structure lacks an FM component, which seems inconsistent with our observation of the FM behavior at 15 K. This discrepancy arises because a weak FM component of ~0.1 μ_B/Mn below 15 K cannot be detected by neutron scattering measurements. Given the small net magnetization and magnetic hysteresis observed in our magnetization measurements, the AFM state of the Type A $Cu_{1-x}Mn_{1+y}SiTe_3$ must involve canting of magnetic moments. Symmetry analysis, based on the *Pm* magnetic space group, indicates that the FM moments are constricted to cant toward the *b* axis, as shown in Fig. 1A.

Although our neutron scattering measurements demonstrate a long-range AFM ordering below 35 K, we observed a frequency-dependent peak in χ' below 35 K, which is suggestive of a glassy magnetic state. The glassy magnetic behavior was also probed through magnetization relaxation measurements (see note S9 and fig. S14). The most probable origin is coexistence of a long-range AFM order and a cluster spin glass state. Considering that there exist Cu and Mn mixing at the Cu1 and Cu2 sites (see table S2) as well as the stacking faults, the resulting disorders, combined with the strong magnetic frustration implied by the large difference between T_{cw} (= −143 K) and T_N (= 35 K), may generate magnetic glassy behavior in some local regions. The chemical valence of Cu is found to be 1+ by x-ray photoelectron spectroscopy (XPS) measurements (see note S10 and fig. S15), meaning that Cu is nonmagnetic and the magnetism of $Cu_{1-x}Mn_{1+y}SiTe_3$ originates from Mn cations.

The magnetic transition at T_N is also manifested in the temperature dependence of resistivity of the $Cu_{1-x}Mn_{1+y}SiTe_3$ sample (S#2) (Fig. 4D). At temperatures above T_N, the resistivity shows a semiconducting behavior, consistent with the optical bandgap noted above and DFT band structure calculations (see note S6). As the temperature drops below T_N, the resistivity initially exhibits a metallic behavior but then transitions to an insulating behavior below 15 K. These observations suggest the electronic structure of $Cu_{1-x}Mn_{1+y}SiTe_3$ is strongly coupled to magnetism.

Magnetodielectric and magnetoelectric effects of $Cu_{1-x}Mn_{1+y}SiTe_3$

Polar magnetic materials such as $Cu_{1-x}Mn_{1+y}SiTe_3$ are expected to show magnetodielectric and magnetoelectric effects, as in multiferroic oxides $BiFeO_3$, $TbMnO_3$, and $CaBaCo_4O_7$ (*8–10*, *41*, *42*). To determine whether $Cu_{1-x}Mn_{1+y}SiTe_3$ has these properties, we measured its temperature-dependent dielectric constant perpendicular to the *ab* plane (ε_r), magnetodielectric constant, and magnetocurrent on the $Cu_{1-x}Mn_{1+y}SiTe_3$ sample (S#2). From these measurements, we found that the Type A $Cu_{1-x}Mn_{1+y}SiTe_3$ exhibits large magnetodielectric and magnetoelectric effects. Figure 5A shows temperature-dependent ε_r measured within the frequency range of 1 to 100 kHz. We found that ε_r exhibits a large anomaly near the AFM transition at T_N; it starts to increase sharply at T_N and then shows a peak at ~20 K before it steeply drops. Although ε_r decreases with the increase in frequency as expected, the ε_r peak position shows almost no frequency dependence below T_N.

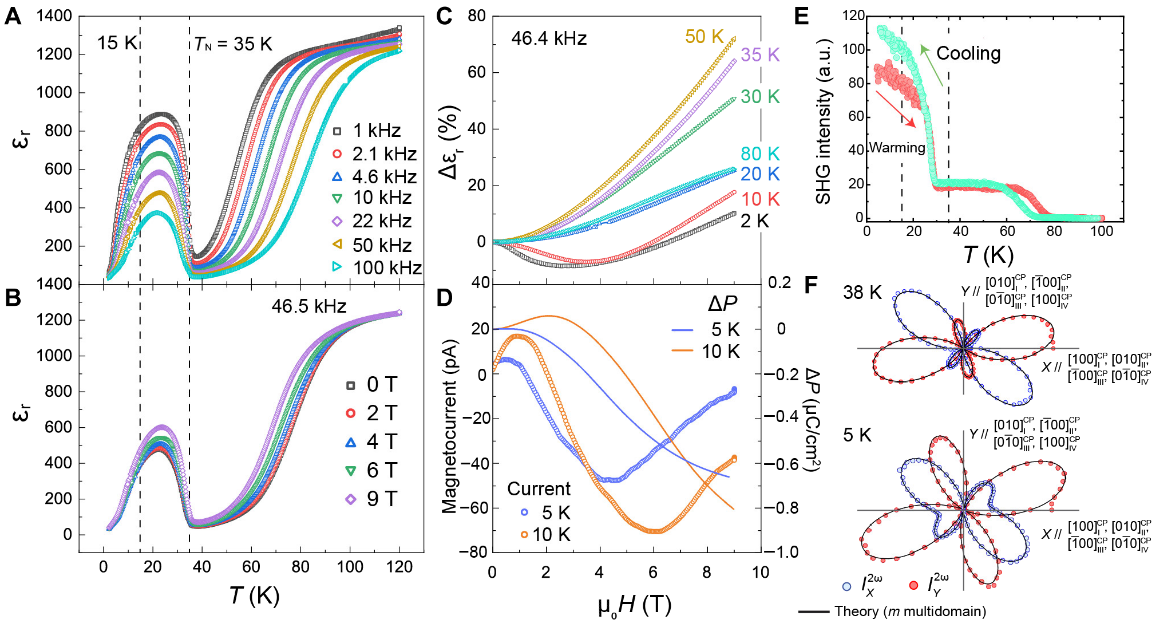

Fig. 5. Magnetodielectric and magnetoelectric effect measurements on $Cu_{0.80}Mn_{1.03}SiTe_{2.92}$ (S#2). Temperature dependence of the dielectric constant perpendicular to the *ab* plane (ε_r) (**A**) at various frequencies and (**B**) magnetic fields. (**C**) Magnetodielectric constant, $\Delta\varepsilon / \varepsilon = [\varepsilon(H) - \varepsilon(0)] / \varepsilon(0)$, as a function of magnetic field at various temperatures. (**D**) Magnetocurrent recorded by sweeping the magnetic field at 5 and 10 K (left axis). Change in the electric polarization (ΔP) induced by applying a magnetic field at 5 and 10 K. (**E**) Temperature dependence of the SHG intensity. Note that the SHG signal is still observable above 80 K as plotted in Fig. 2B. (**F**) Polar plots for the *X*- and *Y*-polarized SHG intensity at 5 and 38 K.

When the magnetic fluctuations in $Cu_{1-x}Mn_{1+y}SiTe_3$, which is implied by the short-range magnetic order, are combined with strong magnetodielectric coupling, one can expect a glassy behavior for the electric dipoles. The step seen in the temperature-variable data of ε_r above T_N depends on the frequency and shifts from ~60 to ~100 K as the frequency increases from 1 to 100 kHz. We also measured the temperature dependences of ε_r under various magnetic fields at 46.5 kHz, observing step shifts toward lower temperatures as the magnetic field increased (Fig. 5B). This magnetic field dependence corroborates the strong correlation between magnetism and electric dipoles in $Cu_{1-x}Mn_{1+y}SiTe_3$, which also implies a strong spin-lattice coupling that could arise through the orbital degree of freedom or from an exchange striction mechanism in this polar magnet (*42*).

We have also measured the magnetodielectric constant $\Delta\varepsilon_r$, defined as $\Delta\varepsilon_r = [\varepsilon_r(H) - \varepsilon_r(0)]/\varepsilon_r(0)$, as a function of magnetic field at various temperatures (Fig. 5C). The Type A $Cu_{1-x}Mn_{1+y}SiTe_3$ displays a significant positive magnetodielectric effect ($\Delta\varepsilon_r$ ~ 50 to 75% at 9 T) in the temperature range of 30 to 50 K, and it decreases with further increasing the temperature. Typically, magnetic insulators/semiconductors with ferroelectricity (e.g., $Fe_2Mo_3O_8$ and $CaBaCo_4O_7$) (*10*, *43*, *44*) show a few percent of magnetodielectric constant near the magnetic transition temperature. A giant $\Delta\varepsilon_r$ was, on the other hand, observed in spin-induced multiferroics with a large magnetoelectric coupling. For instance, multiferroic rare-earth manganite (Dy/Tb)MnO_3 was found to have $\Delta\varepsilon_r$ as high as 500% near its spin-flop transition field (*45*). Similarly, the large $\Delta\varepsilon_r$ value observed in the Type A $Cu_{1-x}Mn_{1+y}SiTe_3$ in conjunction with its ε_r anomaly peak near T_N (Fig. 5A) implies that its AFM ordering induces additional component of ferroelectric polarization and would enhance the ferroelectric polarization; note that $Cu_{1-x}Mn_{1+y}SiTe_3$ already exhibits finite electric polarization at room temperature as shown above. We also noted a crossover transition from a positive to negative magnetodielectric effect in the low field range (<6 T) as the temperature is lowered below 15 K. The change in the direction of the magnetically induced electric polarization due to spin canting is a likely explanation for the crossover transition.

Through measuring magnetocurrent (*10*, *46*), which is a current flow under a magnetic field sweeping with zero electric field, we demonstrate that $Cu_{1-x}Mn_{1+y}SiTe_3$ also exhibits a strong magnetoelectric effect. The time integration of such a current corresponds to the magnetic field–induced electric polarization. This can be attributed to the change of electric polarization due to the magnetic field (ΔP), which is often measured for characterizing type II multiferroics or polar magnets (*10*, *47*, *48*). Figure 5D (right axis) shows ΔP extracted for $Cu_{1-x}Mn_{1+y}SiTe_3$ as a function of the magnetic field. The ΔP reaches ~0.8 $\mu C/cm^2$ at 10 K and 9 T, comparable to the record value of magnetic field–induced polarization in oxide multiferroics (see table S4 for comparison). Such a large ΔP indicates strong magnetoelectric coupling and, combined with the strong magnetodielectric discussed above, suggests that the Type A $Cu_{1-x}Mn_{1+y}SiTe_3$ is multiferroic in its AFM phase. This is further evidenced by the temperature dependence of the SHG intensity shown in Fig. 5E, which shows not only a clear enhancement as the short-range magnetic order develops between T_N and 60 K but also a sharp increase when the long-range AFM order forms below T_N. Because the SHG intensity in ferroelectrics is proportional to the square of the spontaneous polarization, this indicates a strong coupling between the ferroelectric and magnetic orders. Figure 5F shows oblique incidence SHG polar plots measured above and below T_N at 38 and 5 K, respectively which can be fitted to a multidomain *m* model consistent with space group Pm (see supplementary note S4).

Given that $Cu_{1-x}Mn_{1+y}SiTe_3$ exhibits a canted AFM state below 35 K, with its FM component producing net magnetization and magnetic hysteresis (Fig. 4E), this material offers a rare opportunity to investigate multiferroics in layered chalcogenides. We also conducted magnetocurrent measurements at temperatures near T_N, but the measured current strongly fluctuated likely due to the semiconductor-to-metal transition between 15 K and T_N (Fig. 4D). Nevertheless, below 15 K, the system changes into an insulating state, which makes the magnetocurrent measurements possible. The origin of such an insulating state is yet to be clarified.

DISCUSSION

$Cu_{1-x}Mn_{1+y}SiTe_3$ is not categorized into type II multiferroics because the nonmagnetic phase already has a polar structure. Instead, modulation of electric polarization was observed for $Cu_{1-x}Mn_{1+y}SiTe_3$ concomitant with long-range magnetic ordering, whose origin is worth to be investigated. One possibility for the polarization change is the magnetostriction effect. In addition, inverse Dzyaloshinskii-Moriya, exchange striction, and spin-dependent p-d hybridization mechanisms, which result in the emergence of macroscopic polarization in type II multiferroics, are other possible mechanisms. Further systematic study is needed to unambiguously determine which mechanism operates. Anyhow, we anticipate that this layered chalcogenide, with both electric polarization and net magnetization, can open up an unexplored class of multiferroic chemistry.

MATERIALS AND METHODS

Single-crystal growth

Single crystals of $Cu_{1-x}Mn_{1+y}SiTe_3$ were synthesized by using the melt-growth method. A mixture of Mn (99.95%), Cu (99.95%), Si (99.999%), and Te (99.999%) in a molar ratio of 1:1:1:3 was placed in a canfield crucible assembly. The crucible assembly was sealed in an evacuated quartz ampoule after three times purging with high-purity Ar. The ampoule was first heated in a muffle furnace up to 1000°C for 12 hours and maintained at this temperature for 24 hours to obtain a homogeneous melt. Subsequently, the furnace was slowly cooled to 800°C over 40 hours, then to 650°C over 120 hours, and held at 650°C for 24 hours to anneal the crystals. The obtained crystals were black, shiny, and plate-like with typical dimensions of 2 mm by 2 mm by 0.5 mm. The crystal compositions are analyzed using EDXS. The measured compositions are nonstoichiometric, expressed as $Cu_{1-x}Mn_{1+y}SiTe_3$, with $0.04 \le x < 0.26$ and $0.03 \le y \le 0.15$, with an average composition of $Cu_{0.82}Mn_{1.08}SiTe_{2.99}$ (see note S1 and table S1). In addition, we find that the composition of this compound can be tuned by adjusting the nominal starting ratios. For instance, using $Cu_{1.4}Mn_{0.6}SiTe_3$ or $Cu_{1.2}Mn_{0.8}SiTe_3$ as nominal compositions, the EDXS-measured average compositions of the grown crystals are $Cu_{1.15}Mn_{0.80}SiTe_{2.91}$ and $Cu_{0.96}Mn_{0.98}SiTe_{2.90}$, respectively (see note S1 and table S1). This paper focuses solely on crystals grown with the nominal composition $CuMnSiTe_3$, resulting in measured compositions of $Cu_{1-x}Mn_{1+y}SiTe_3$ ($0.04 \le x < 0.26$; $0.03 \le y \le 0.15$) as only samples within this range exhibit multiferroic properties.

The single crystals used in our initial neutron and STEM studies were grown using the Te-flux method with a molar ratio of

Cu:Mn:Si:Te = 1:1:1:6. The mixed source materials were also sealed in evacuated quartz ampoules, heated up to 1000°C and maintained at this temperature for 24 hours and then slowly cooled down to 650°C over 175 hours. After annealing at 650°C for 12 hours, the ampoules were quickly removed from the furnace and centrifuged to separate the crystals from the Te flux. The Te-flux grown crystals are less homogeneous than the melt-grown ones and exhibit a higher density of stacking faults in some pieces. All the measurements presented in this paper are based on melt-grown crystals.

Single-crystal neutron diffraction

Single-crystal neutron diffraction measurements were conducted at the single-crystal diffractometer TOPAZ, located at the Oak Ridge National Laboratory, United States (*49*). A piece of single crystal with a mass of ~17 mg (S#1) was selected for full dataset collection at 300, 293, 50, 23, and 4 K. A CryoStream 700 Plus was used to collect the data at 293 K, whereas a cryogenic goniometer was adapted to cover the temperature region in 4 K < T < 300 K for data collection at other temperatures. The crystal was rotated through a wide angle for survey on the elastic peaks in a wide range of reciprocal space. The temperature dependence of some nuclear/magnetic peaks was measured by a data collection with a slow ramping rate of 0.6 K/min in the temperature ranging from 4 to 35 K. Neutron data were reduced by Mantid (*50*), and the integrated intensities of the Bragg peaks were obtained using the Python scripts available (*51*) at TOPAZ. We used the crystallographic computing system JANA to determine the crystal structure.

Optical bandgap measurements

Because the crystal is monoclinic, it has four nonzero elements in the optical constant tensor, and its crystallographic, crystal physics, and principle coordinates do not coincide with one another (*52*, *53*). Therefore, in this geometry, the effective optical constants $\widetilde{n}_{\mathrm{eff}} = n + ik$ involving $\widetilde{n}_{11}$, $\widetilde{n}_{22}$, and $\widetilde{n}_{13}$ were probed and extracted by fitting the ellipsometry data to four Lorentz oscillators. The absorption coefficient, a, can then be found using the equation: $a = 4\pi k / \lambda$, in which λ is the wavelength of light.

Spectroscopic ellipsometry was performed to determine the optical bandgap of the Type A $Cu_{1-x}Mn_{1+y}SiTe_3$ (S#2). The ellipsometry spectrum was measured at an incident angle of 65° on the (001) plane of the crystal from 0.85 to 5 eV using a variable-angle rotating-compensator multichannel spectroscopic ellipsometer (M-2000 ellipsometer, Woollam). The ellipsometry spectrum was fitted to four Lorentz oscillators to extract the optical constants and absorption coefficient. Each Lorentz oscillator consists of an amplitude A, broadening parameter B, and central transition energy E_0. The bandgap can be related to the absorption coefficient by $(\alpha h\nu)^{1/n} = A\left(h\nu + E_p - E_g\right)$. Here, A is a proportionality factor, h is the Planck's constant, and n = 0.5 or 2 for direct and indirect bandgap, respectively (*54*, *55*), which, in this case, is 2. E_p represents the phonon energy needed for the momentum transition ($E_p = 0$ for direct bandgap). However, it is negligible in most cases (*56*) and therefore taken as zero here. The indirect and direct bandgap can then be found by extrapolating the linear region of the curve to $(\alpha h\nu)^{0.5} = 0$ and $(\alpha h\nu)^2 = 0$, respectively.

Optical SHG measurements

The SHG polarimetry measurements at room temperature were performed on a modified Witec Alpha 300S confocal microscope in far-field reflection geometry, using an 800-nm fundamental laser beam generated by a Spectra-Physics SOLSTICE ACE Ti:sapphire femtosecond laser system (pulse width of ~100 fs and repetition rate of 80 MHz). A half-wave plate was used to control the polarization direction (φ) of the incident field (E^{ω}). The second-harmonic field ($E^{2\omega}$) generated through the nonlinear optical process inside the sample was first spectrally filtered and then decomposed parallel to either lab X or Y axis by an analyzer and lastly detected by a photomultiplier tube. The schematic of our setup is shown in Fig. 2A.

For temperature-dependent SHG measurements, an oblique incidence SHG setup is used because it is sensitive to both in-plane and out-of-plane polarization components. The schematic of the SHG setup is shown in fig. S9. A regeneratively amplified 800-nm fundamental laser beam from a Ti:sapphire system (pulse width of ~100 fs and repetition rate ~1 kHz) was used as the fundamental beam. Temperature control was achieved through a Janis 300 gas flow cryostat.

Scanning transmission electron microscopy

STEM experiments were performed to confirm the crystal structure. The orientation of the crystal was determined using Laue diffraction and lamella was extracted along the [010] zone axis using focused ion beam (FIB). A Thermo Fisher Scientific Helios 660 NanoLab Dual-Beam FIB was used to thin the sample for electron transparency. STEM images were acquired at an 80-kV accelerating voltage using an aberration-corrected Thermo Fisher Scientific Titan G2 microscope. Bandpass filter was applied to the ADF-STEM image. The selected-area electron diffraction in fig. S4 was acquired at a 200-kV accelerating voltage using Talos X 200.

Piezoresponse force microscopy

All PFM measurements were deployed via an Oxford Instruments Asylum Research Cypher atomic force microscope. All measurements were performed under ambient conditions under standard humid conditions (about 20 to 50%). Band excitation PFM was collected using an ac voltage of 1 V. All experiments used Budget Sensor Multi75E-G Cr/Pt-coated AFM probes (~3 N/m).

Computational method

The DFT calculation is done by The Vienna Ab initio Simulation Package (VASP) (*57*–*60*), at the level of Perdew-Burke-Ernzerhof (PBE) (*61*) with a cutoff energy of 600 eV and a 7 by 7 by 3 Monkhorst-Pack mesh (*62*). The Hubbard U values of 3.9 eV for Mn and 7.2 eV for Cu used in the rotationally invariant DFT + U method (*63*) are from (*64*, *65*), where the metal atoms are coordinated similarly by chalcogen atoms. The k-path for the band structure calculation is determined using pymatgen (*66*, *67*).

Magnetic, heat capacity, resistivity, dielectric constant, and magnetocurrent measurements

Magnetic measurements were performed in a vibrating-sample SQUID magnetometer (Quantum Design, SQUID-VSM). Heat capacity, four-probe resistivity, dielectric constant, and magnetocurrent were measured in the Physical Property Measurement System (Quantum Design). For dielectric constant and magnetocurrent measurement, flat plate-like samples were chosen to put electrodes on both sides using single component silver paint. Temperature-dependent and magnetic field–dependent capacitance was measured using an

Agilent E4980A Precision LCR meter, and the dielectric constant was derived from the measured capacitance value. Magnetocurrent was recorded using a Keithley electrometer 6517B. For these magnetocurrent measurements, the sample was first cooled from 50 K (above T_N) to 5 K under an electric field of 2 kV/cm and a magnetic field of 9 T perpendicular to the *ab* plane. At 5 K, the electric field was removed, and the electrodes were kept shorted for 30 min to remove the stray charges. Then, the electrometer was connected to the sample, and the current was recorded while ramping the magnetic field from 9 to 0 T at a rate of 100 Oe/s. The recorded current was integrated with the time to obtain the electric polarization of the sample. A similar procedure was applied to record the magnetocurrent at 10 K where the sample was poled from 50 to 10 K.

XPS measurements

XPS measurements were performed at room temperature with a Physical Electronics Quantera SXM Scanning X-ray Microprobe. This system uses a focused monochromatic Al K_α x-ray (1486.7 eV) source for excitation and a spherical section analyzer. The instrument has a 32-element multichannel detection system. The x-ray beam was incident normal to the sample, and the photoelectron detector is at 45° off-normal. High-energy resolution spectra were collected using a pass energy of 69.0 eV with a step size of 0.125 eV. For the Ag $3d_{5/2}$ line, these conditions produced a full width at half maximum of 0.92 ± 0.05 eV. The binding energy scale is calibrated using the Cu $2p_{3/2}$ feature at 932.62 ± 0.05 eV and Au $4f_{7/2}$ at 83.96 ± 0.05 eV. Low-energy electrons at ~1 eV and 20 μA as well as low-energy Ar^+ ions were used to minimize sample charging during analysis.

Supplementary Materials

This PDF file includes:
Notes S1 to S10
Figs. S1 to S15
Tables S1 to S4
References

REFERENCES AND NOTES

1. D. Zhang, P. Schoenherr, P. Sharma, J. Seidel, Ferroelectric order in van der Waals layered materials. *Nat. Rev. Mater.* **8**, 25–40 (2023).
2. C. Paillard, X. Bai, I. C. Infante, M. Guennou, G. Geneste, M. Alexe, J. Kreisel, B. Dkhil, Photovoltaics with ferroelectrics: Current status and beyond. *Adv. Mater.* **28**, 5153–5168 (2016).
3. K. Uchino, *Ferroelectric Devices* (CRC Press, 2018).
4. S. Das, Z. Hong, M. McCarter, P. Shafer, Y.-T. Shao, D. A. Muller, L. W. Martin, R. Ramesh, A new era in ferroelectrics. *APL Mater.* **8**, 120902 (2020).
5. S.-W. Cheong, M. Mostovoy, Multiferroics: A magnetic twist for ferroelectricity. *Nat. Mater.* **6**, 13–20 (2007).
6. N. A. Hill, Why are there so few magnetic ferroelectric? *J. Phys. Chem. B* **104**, 6694–6709 (2000).
7. N. A. Spaldin, R. Ramesh, Advances in magnetoelectric multiferroics. *Nat. Mater.* **18**, 203–212 (2019).
8. J. Wang, J. B. Neaton, H. Zheng, V. Nagaraja, S. B. Ogale, B. Liu, D. Viehland, D. G. Schlom, U. V. Waghmare, N. A. Spaldin, K. M. Rabe, M. Muttig, R. Ramesh, Epitaxial $BiFeO_3$ multiferroic thin film heterostructures. *Science* **299**, 1719–1722 (2003).
9. T. Kimura, T. Goto, H. Shintani, K. Ishizaka, T. Arima, Y. Tokura, Magnetic control of ferroelectric polarization. *Nature* **426**, 55–58 (2003).
10. Y. Wang, G. L. Pascut, B. Gao, T. A. Tyson, K. Haule, V. Kiryukhin, S.-W. Cheong, Unveiling hidden ferrimagnetism and giant magnetoelectricity in polar magnet $Fe_2Mo_3O_8$. *Sci. Rep.* **5**, 12268 (2015).
11. S. Ghara, E. Suard, F. Fauth, T. T. Tran, P. S. Halasyamani, A. Iyo, J. Eodríguez-Carvajal, A. Sundaresan, Ordered aeschynite-type polar magnets RFeWO$_6$ (R = Dy, Eu, Tb, and Y): A new family of type-II multiferroics. *Phys. Rev. B* **95**, 224416 (2017).
12. E. A. Eliseev, S. V. Kalinin, A. N. Morozovska, Finite size effects in ferroelectric-semiconductor thin films under open-circuit electric boundary conditions. *J. Appl. Phys.* **117**, 034102 (2015).
13. J. Junquera, P. Ghosez, Critical thickness for ferroelectricity in perovskite ultrathin films. *Nature* **422**, 506–509 (2003).
14. A. Jindal, A. Saha, Z. Li, T. Taniguchi, K. Watanabe, J. C. Hone, T. Birol, R. M. Fernandes, C. R. Dean, A. N. Pasupathy, D. A. Rhodes, Coupled ferroelectricity and superconductivity in bilayer T_d-$MoTe_2$. *Nature* **613**, 48–52 (2023).
15. S. Yuan, X. Luo, H. L. Chan, C. Xiao, Y. Dai, M. Xie, J. Hao, Room-temperature ferroelectricity in $MoTe_2$ down to the atomic monolayer limit. *Nat. Commun.* **10**, 1775 (2019).
16. F. Sui, M. Jin, Y. Zhang, R. Qi, Y.-N. Wu, R. Huang, F. Yue, J. Chu, Sliding ferroelectricity in van der Waals layered γ-InSe semiconductor. *Nat. Commun.* **14**, 36 (2023).
17. L.-P. Miao, N. Ding, N. Wang, C. Shi, H.-Y. Ye, L. Li, Y.-F. Yao, S. Dong, Y. Zhang, Direct observation of geometric and sliding ferroelectricity in an amphidynamic crystal. *Nat. Mater.* **21**, 1158–1164 (2022).
18. Z. Fei, W. Zhao, T. A. Palomaki, B. Sun, M. K. Miller, Z. Zhao, J. Yan, X. Xu, D. Cobden, Ferroelectric switching of a two-dimensional metal. *Nature* **560**, 336–339 (2018).
19. K. Yasuda, X. Wang, K. Watanabe, T. Taniguchi, P. Jarillo-Herrero, Stacking-engineered ferroelectricity in bilayer boron nitride. *Science* **372**, 1458–1462 (2021).
20. E. Y. Andrei, D. Efetov, P. Jarillo-Herrero, A. H. MacDonald, K. F. Mak, T. Senthil, E. Tutuc, A. Yazdani, A. F. Young, The marvels of moiré materials. *Nat. Rev. Mater.* **6**, 201–206 (2021).
21. F. Liu, L. You, K. L. Seyler, X. Li, P. Yu, J. Lin, X. Wang, J. Zhou, H. Wang, H. He, S. T. Panelides, W. Zhou, P. Sharma, X. Xu, P. M. Ajayan, J. Wang, Z. Liu, Room-temperature ferroelectricity in $CuInP_2S_6$ ultrathin flakes. *Nat. Commun.* **7**, 12357 (2016).
22. X. Wang, K. Yasuda, Y. Zhang, S. Liu, K. Watanabe, T. Tanguchi, J. Hone, L. Fu, P. Jarillo-Herrero, Interfacial ferroelectricity in rhombohedral-stacked bilayer transition metal dichalcogenides. *Nat. Nanotechnol.* **17**, 367–371 (2022).
23. S. Barraza-Lopez, B. M. Fregoso, J. W. Villanova, S. S. P. Parkin, K. Chang, *Colloquium*: Physical properties of group-IV monochalcogenide monolayers. *Rev. Mod. Phys.* **93**, 011001 (2021).
24. M. Xu, C. Huang, Y. Li, S. Liu, X. Zhang, P. Jena, E. Kan, Y. Wang, Electrical control of magnetic phase transition in a type-I multiferroic double-metal trihalide monolayer. *Phys. Rev. Lett.* **124**, 067602 (2020).
25. J.-J. Zhang, L. Lin, Y. Zhang, M. Wu, B. I. Yakobson, S. Dong, Type-II multiferroic $Hf_2VC_2F_2$ MXene monolayer with high transition temperature. *J. Am. Chem. Soc.* **140**, 9768–9773 (2018).
26. C. Huang, Y. Du, H. Wu, H. Xiang, K. Deng, E. Kan, Prediction of intrinsic ferromagnetic ferroelectricity in a transition-metal halide monolayer. *Phys. Rev. Lett.* **120**, 147601 (2018).
27. C. Wang, L. You, D. Cobden, J. Wang, Towards two-dimensional van der Waals ferroelectrics. *Nat. Mater.* **22**, 542–552 (2023).
28. K. F. Mak, J. Shan, D. C. Ralph, Probing and controlling magnetic states in 2D layered magnetic materials. *Nat. Rev. Phys.* **1**, 646–661 (2019).
29. Q. Song, C. A. Occhialini, E. Ergecen, B. Ilyas, D. Amoroso, P. Barone, J. Kapeghian, K. Watanabe, T. Taniguchi, A. S. Botana, S. Picozzi, N. Gedik, R. Comin, Evidence for a single-layer van der Waals multiferroic. *Nature* **602**, 601–605 (2022).
30. T. Kurumaji, S. Seki, S. Ishiwata, H. Murakawa, Y. Kaneko, Y. Tokura, Magnetoelectric responses induced by domain rearrangement and spin structural change in triangular-lattice helimagnets NiI_2 and CoI_2. *Phys. Rev. B* **87**, 014429 (2013).
31. S. P. Poudel, J. M. Marmolejo-Tejada, J. E. Roll, M. A. Mosquera, S. Barraza-Lopez, Creating a three-dimensional intrinsic electric dipole on rotated CrI_3 bilayers. *Phys. Rev. B* **107**, 195128 (2023).
32. X. Liu, A. P. Pyatakov, W. Ren, Magnetoelectric coupling in multiferroic bilayer VS_2. *Phys. Rev. Lett.* **125**, 247601 (2020).
33. C. Xu, P. Chen, H. Tan, Y. Yang, H. Xiang, L. Bellaiche, Electric-field switching of magnetic topological charge in Type-I multiferroics. *Phys. Rev. Lett.* **125**, 037203 (2020).
34. T. Zhong, X. Li, M. Wu, J.-M. Liu, Room-temperature multiferroicity and diversified magnetoelectric couplings in 2D materials. *Natl. Sci. Rev.* **7**, 373–380 (2020).
35. C. B. Park, A. Shahee, K.-T. Kim, D. R. Patil, S. A. Guda, N. Ter-Oganessian, K. H. Kim, Observation of spin-induced ferroelectricity in a layered van der Waals antiferromagnet $CuCrP_2S_6$. *Adv. Electron. Mater.* **8**, 2101072 (2022).
36. W. F. Io, S.-Y. Pang, L. W. Wong, Y. Zhao, R. Ding, J. Mao, Y. Zhao, F. Guo, S. Yuan, J. Zhao, J. Yi, J. Hao, Direct observation of intrinsic room-temperature ferroelectricity in 2D layered $CuCrP_2S_6$. *Nat. Commun.* **14**, 7304 (2023).
37. G. Cardenas-Chirivi, K. Vega-Bustos, H. Rojas-Páez, D. Silvera-Vega, J. Pazos, O. Herrera, M. A. Macías, C. Espejo, W. López-Pérez, J. A. Galvis, P. Giraldo-Gallo, Room temperature multiferroicity in a transition metal dichalcogenide. *npj 2D Mater. Appl.* **7**, 54 (2023).
38. Y. Jiang, Y. Wu, J. Zhang, J. Wei, B. Peng, C.-W. Qiu, Dilemma in optical identification of single-layer multiferroics. *Nature* **619**, E40–E43 (2023).
39. X. Wang, Z. Shang, C. Zhang, J. Kang, T. Liu, X. Wang, S. Chen, H. Liu, W. Tang, Y.-J. Zeng, J. Guo, Z. Cheng, L. Liu, D. Pan, S. Tong, B. Wu, Y. Xie, G. Wang, J. Deng, T. Zhai, H.-X. Deng,

J. Hong, J. Zhao, Electrical and magnetic anisotropies in van der Waals multiferroic $CuCrP_2S_6$. *Nat. Commun.* **14**, 840 (2023).
40. K. Cho, S. Lee, R. Kalaivanan, R. Sankar, K.-Y. Choi, S. Park, Tunable ferroelectricity in van der Waals layered antiferroelectric $CuCrP_2S_6$. *Adv. Funct. Mater.* **32**, 2204214 (2022).
41. R. S. P. N, S. Mishra, S. Athinarayanan, Polar magnetic oxides from chemical ordering: A new class of multiferroics. *APL Mater.* **8**, 040906 (2020).
42. V. Kocsis, Y. Tokunaga, T. Rõõm, U. Nagel, J. Fujioka, Y. Taguchi, Y. Tokura, S. Bordács, Spin-lattice and magnetoelectric couplings enhanced by orbital degrees of freedom in polar multiferroic semiconductors. *Phys. Rev. Lett.* **130**, 036801 (2023).
43. V. Caignaert, A. Maignan, K. Singh, C. Simon, V. Pralong, B. Raveau, J. F. Mitchell, H. Zheng, A. Huq, L. C. Chapon, Gigantic magnetic-field-induced polarization and magnetoelectric coupling in a ferrimagnetic oxide $CaBaCo_4O_7$. *Phys. Rev. B* **88**, 174403 (2013).
44. J. K. Harada, L. Balhorn, J. Hazi, M. C. Kemei, R. Seshadri, Magnetodielectric coupling in the ilmenites MTiO$_3$ (M = Co, Ni). *Phys. Rev. B* **93**, 104404 (2016).
45. T. Goto, T. Kimura, G. Lawes, A. P. Ramirez, Y. Tokura, Ferroelectricity and giant magnetocapacitance in perovskite rare-earth manganites. *Phys. Rev. Lett.* **92**, 257201 (2004).
46. I. Kézsmárki, S. Bordács, P. Milde, E. Neuber, L. M. Eng, J. S. White, H. M. Rønnow, C. D. Dewhurst, M. Mochizuki, K. Yanai, H. Nakamura, D. Ehlers, V. Tsurkan, A. Loidl, Néel-type skyrmion lattice with confined orientation in the polar magnetic semiconductor GaV_4S_8. *Nat. Mater.* **14**, 1116–1122 (2015).
47. K. Singh, C. Simon, E. Cannuccia, M.-B. Lepetit, B. Corraze, E. Janod, L. Cario, Orbital-ordering-driven multiferroicity and magnetoelectric coupling in GeV_4S_8. *Phys. Rev. Lett.* **113**, 137602 (2014).
48. E. Ruff, S. Widmann, P. Lunkenheimer, V. Tsurkan, S. Bordács, I. Kézsmárki, A. Loidl, Multiferroicity and skyrmions carrying electric polarization in GaV_4S_8. *Sci. Adv.* **1**, e1500916 (2015).
49. L. Coates, H. B. Cao, B. C. Chakoumakos, M. D. Frontzek, C. Hoffmann, A. Y. Kovalevsky, Y. Liu, F. Meilleur, A. M. Dos Santos, D. A. A. Myles, X. P. Wang, F. Ye, A suite-level review of the neutron single-crystal diffraction instruments at Oak Ridge National Laboratory. *Rev. Sci. Instrum.* **89**, 092802 (2018).
50. O. Arnold, J. C. Bilheux, J. M. Borreguero, A. Buts, S. I. Campbell, L. Chapan, M. Doucet, N. Draper, R. Ferraz Leal, M. A. Gigg, V. E. Lynch, A. Markvardsen, D. J. Mikkelson, R. L. Mikkelson, R. Miller, K. Palmen, P. Parker, G. Passos, T. G. Perring, P. F. Peterson, S. Ren, M. A. Reuter, A. T. Savici, J. W. Taylor, R. J. Taylor, R. Tolchenov, W. Zhou, J. Zikovsky, Mantid—Data analysis and visualization package for neutron scattering and μSR experiments. *Nucl. Instrum. Methods Phys. Res. A* **764**, 156–166 (2014).
51. A. J. Schultz, M. R. V. Jørgensen, X. Wang, R. L. Mikkelson, D. J. Mikkelson, V. E. Lynch, P. F. Peterson, M. L. Green, C. M. Hoffmann, Integration of neutron time-of-flight single-crystal Bragg peaks in reciprocal space. *J. Appl. Cryst.* **47**, 915–921 (2014).
52. A. Halevy, E. Megidish, L. Dovrat, H. S. Eisenberg, P. Becker, L. Bohaty, The biaxial nonlinear crystal BiB_3O_6 as a polarization entangled photon source using non-collinear type-II parametric down-conversion. *Opt. Express* **19**, 20420–20434 (2011).
53. J. He, A. K. Iyer, M. J. Waters, S. Sarkar, R. Zu, J. M. Rondinelli, M. G. Kanatzidis, V. Gopalan, Giant non-resonant infrared second order nonlinearity in γ-$NaAsSe_2$. *Adv. Opt. Mater.* **10**, 2101729 (2022).
54. J. Tauc, Optical properties and electronic structure of amorphous Ge and Si. *Mater. Res. Bull.* **3**, 37–46 (1968).
55. P. Y. Yu, M. Cardona, *Fundamentals of Semiconductors: Physics and Materials Properties* (Springer: Berlin/Heidelberg, 2010).
56. A. R. Zanatta, Revisiting the optical bandgap of semiconductors and the proposal of a unified methodology to its determination. *Sci. Rep.* **9**, 11225 (2019).
57. G. Kresse, J. Hafner, Ab initio molecular dynamics for liquid metals. *Phys. Rev. B* **47**, 558–561 (1993).
58. G. Kresse, J. Furthmüller, Efficiency of ab-initio total energy calculations for metals and semiconductors using a plane-wave basis set. *Comput. Mater. Sci.* **6**, 15–50 (1996).
59. G. Kresse, D. Joubert, From ultrasoft pseudopotentials to the projector augmented-wave method. *Phys. Rev. B* **59**, 1758–1775 (1999).
60. G. Kresse, J. Furthmüller, Efficient iterative schemes for ab initio total-energy calculations using a plane-wave basis set. *Phys. Rev. B* **54**, 11169–11186 (1996).
61. J. P. Perdew, K. Burke, M. Ernzerhof, Generalized gradient approximation made simple. *Phys. Rev. Lett.* **77**, 3865–3868 (1996).
62. H. J. Monkhorst, J. D. Pack, Special points for Brillouin-zone integrations. *Phys. Rev. B* **13**, 5188–5192 (1976).
63. A. I. Liechtenstein, V. I. Anisimov, J. Zaanen, Density-functional theory and strong interactions: Orbital ordering in Mott-Hubbard insulators. *Phys. Rev. B* **52**, R5467–R5470 (1995).
64. D. Durkee, D. Smith, R. Torchio, S. Petitgirard, R. Briggs, I. Kantor, S. R. Evans, T. Chatterji, T. Irifune, S. Pascarelli, K. V. Lawler, A. Salamat, S. A. J. Kimber, Electronic origins of the giant volume collapse in the pyrite mineral MnS_2. *J. Solid State Chem.* **269**, 540–546 (2019).
65. X. Wu, C. Ming, W. Gao, J. Shi, K. Zhao, H. Wang, Y.-Y. Sun, Effect of liquidlike cations on electronic and defect properties of solid solutions of Cu_2Te and Ag_2Te. *Phys. Rev. B* **105**, 195206 (2022).
66. S. P. Ong, W. D. Richards, A. Jain, G. Hautier, M. Kocher, S. Cholia, D. Gunter, V. L. Chevrier, K. A. Persson, G. Ceder, Python Materials Genomics (pymatgen): A robust, open-source python library for materials analysis. *Comput. Mater. Sci.* **68**, 314–319 (2013).
67. Y. Hinuma, G. Pizzi, Y. Kumagai, F. Oba, I. Tanaka, Band structure diagram paths based on crystallography. *Comput. Mater. Sci.* **128**, 140–184 (2017).
68. O. V. Dolomanov, L. J. Bourthis, R. J. Gildea, J. A. K. Howard, H. Puschmann, OLEX2: A complete structure solution, refinement, and analysis program. *J. Appl. Cryst.* **42**, 339–341 (2009).
69. G. M. Sheldrick, Crystal structure refinement with *SHELXL*. *Acta Crystallogr. C Struct. Chem.* **71**, 3–8 (2015).
70. J. P. Perdew, M. Levy, Physical content of the exact Kohn-Sham orbital energies: Band gaps and derivative discontinuities. *Phys. Rev. Lett.* **51**, 1884–1887 (1983).
71. S. W. Gaarenstroom, N. Winogard, Initial and final state effects in the ESCA spectra of cadmium and silver oxides. *J. Chem. Phys.* **67**, 3500–3506 (1977).
72. J. Conradie, E. Erasmus, XPS photoelectron lines, satellite structures and Wagner plot of Cu(II) β-diketonato complexes explained in terms of its electronic environment. *J. Electron Spectros. Relat. Phenomena* **259**, 147241 (2022).
73. M. C. Biesinger, Advanced analysis of copper X-ray photoelectron spectra. *Surf. Interface Anal.* **49**, 1325–1334 (2017).
74. E. Ruff, A. Butykai, K. Geirhos, S. Widmann, V. Tsurkan, E. Strfanet, I. Kézsmárki, A. Loidl, P. Lunkenheimer, Polar and magnetic order in GaV_4Se_8. *Phys. Rev. B* **96**, 165119 (2017).
75. M. Tokunaga, M. Akaki, T. Ito, S. Miyahara, A. Miyake, H. Kuwahara, N. Furukawa, Magnetic control of transverse electric polarization in $BiFeO_3$. *Nat. Commun.* **6**, 5878 (2015).
76. Y. Tokunaga, Y. Taguchi, T.-H. Arima, Y. Tokura, Electric-field-induced generation and reversal of ferromagnetic moment in ferrites. *Nat. Phys.* **8**, 838–844 (2012).
77. R. Johnson, K. Cao, F. Giustino, P. Radaelli, $CaBaCo_4O_7$: A ferrimagnetic pyroelectric. *Phys. Rev. B* **90**, 045129 (2014).
78. V. Kocsis, Y. Tokunaga, S. Bordács, M. Kriener, A. Puri, U. Zeitler, Y. Taguchi, Y. Tokura, I. Kézsmárki, Magnetoelectric effect and magnetic phase diagram of a polar ferrimagnet $CaBaFe_4O_7$. *Phys. Rev. B* **93**, 014444 (2016).
79. P. Yanda, S. Mishra, A. Sundaresan, Magnetic-order-induced ferroelectric polarization in the polar antiferromagnets RFeWO$_6$ (R = Sm, Gd, Er, and Tm). *Phys. Rev. Mater.* **5**, 074406 (2021).
80. R. S. P. N, F. Orlandi, P. Manuel, W. Zhang, P. S. Halasyamani, A. Sundaresan, A-site and B-site cation ordering induces polar and multiferroic behavior in the perovskite $NaLnNiWO_6$ (Ln = Y, Dy, Ho, and Yb). *Chem. Mater.* **32**, 5641–5649 (2020).
81. C. De, A. Sundaresan, Nonswitchable polarization and magnetoelectric coupling in the high-pressure synthesized doubly ordered perovskites $NaYMnWO_6$ and $NaHoCoWO_6$. *Phys. Rev. B* **97**, 214418 (2018).

Acknowledgments: The x-ray data were measured on the Rigaku XtaLab Synergy-R DW system housed in the SNS X-ray Diffraction Laboratory. **Funding:** This study is primarily based on research conducted at The Pennsylvania State University Two-Dimensional Crystal Consortium-Materials Innovation Platform (2DCC-MIP), which is supported by NSF Cooperative Agreement No. DMR-2039351. Z.M. also acknowledges the support from the NSF under grant no. DMR 2211327. S.V.G.A. acknowledges the support from the NSF through the Pennsylvania State University Materials Research Science and Engineering Center (MRSEC) DMR-2011839 (2020-2026). N.A., W.X. and S.V.G.A. acknowledge the support from the Experimental Condensed Matter Physics, Division of Materials Sciences and Engineering, Basic Energy Sciences, US DOE, grant no. DE-SC0024943 for the structure study using STEM and XRD. S.G. acknowledges the support from the National Science Foundation award no. DMR-2018579. X.K. acknowledges the support by the US DOE under award no. DE-SC0019259 for partial magnetic measurements. In-vacuum cleave and XPS measurements along with the corresponding analysis were supported by the US Department of Energy (DOE), Office of Science, Basic Energy Sciences, Division of Materials Sciences and Engineering, Synthesis and Processing Science Program, under award no. 10122. S.H. and V.G. acknowledge the support from the DOE, Basic Energy Sciences grant no. DE-SC0012375 for the nonlinear optical characterization. J.H. and V.G. acknowledge the support from the NSF grant no. DMR-2210933 for linear optical characterization. Neutron diffraction research used resources at the Spallation Neutron Source, a DOE Office of Science User Facility operated by the Oak Ridge National Laboratory.The piezoresponse force microscopy research was supported by the Center for Nanophase Materials Sciences (CNMS), which is a US Department of Energy Office of Science User Facility at Oak Ridge National Laboratory. **Author contributions:** C.D. synthesized the neutron and STEM sample in the initial study by using the Te-flux method and the Cu-deficient Type A sample (S#2) using the melt-growth method. Y.L. synthesized the Cu-deficient Type A samples (S#1, S#3, and S#4) as well as the Cu-rich Type B and Type C samples (see note S1 and table S1) by using the melt-growth method. C.D. and S.M. did dielectric constant and pyroelectric current measurements. K.P.K. and C.D. performed PFM measurements. S.V.G.A. and N.A. performed STEM analyses. S.H., S.Y., J.H., and V.G. did optical measurements. S.G. conducted ac magnetic susceptibility measurements. S.Y. contributed to data analyses and initial structure characterization. Y.G., C.D., M.S., and X.K. did magnetization measurements. S.H.L. helped with initial sample growth and transport measurements. L.W., M.H.E., and Y.D. contributed to XPS measurements and analyses. W.X. performed initial single-crystal x-ray diffraction measurements and analyses. B.Z. and V.H.C. analyzed the structural stacking faults and conducted DFT calculations. S.P., X.W., and Q.Z. conducted the single-crystal x-ray diffraction measurements and crystal structure refinements. X.W. and Q.Z. performed the single-crystal neutron scattering measurements and conducted data analysis on crystal and magnetic structures. The manuscript was written by C.D., Y.L., S.Y., V.H.C., V.G., Q.Z., and Z.M. with input from other coauthors. This project was supervised by Z.M. **Competing interests:** The authors declare that they have no competing interests. **Data and materials availability:** All data needed to evaluate the conclusions in the paper are present in the paper and/or the Supplementary Materials. Additional data relevant to this work are stored in the Lifetime Sample Tracking (LiST) Data Management System of the 2D Crystal Consortium (2DCC)–NSF Materials Innovation Platform at https://data.2dccmip.org/3cpW3VVHmUc3.

Submitted 18 April 2024
Accepted 26 November 2024
Published 1 January 2025
10.1126/sciadv.adp9379